Materials Technology Reports 2026, 4(1), 3791.
doi: https://doi.org/10.59400/mtr3791

Article

Method of forming quantum dots for lenses of technical vision cameras in the infrared and ultraviolet ranges

Mortin Konstantin

Digital Steel JSC, Moscow 123100, Russia; mortinkv@ya.ru

CITATION

Konstantin M. Method of forming quantum dots for lenses of technical vision cameras in the infrared and ultraviolet ranges. Materials Technology Reports. 2026; 4(1): 3791.
https://doi.org/10.59400/mtr3791

ARTICLE INFO

Received: 28 November 2025
Revised: 22 April 2026
Accepted: 15 May 2026
Available online: 22 May 2026

Abstract: This paper presents a comprehensive methodology for the formation of quantum dots (QDs) with tailored optical properties, designed for integration into machine vision camera lenses operating in the ultraviolet radiation (UV) and infrared radiation (IR) spectral ranges. Based on a self-consistent solution of the Schrödinger–Poisson equations and the non-equilibrium Green's function (NEGF) formalism, a predictive model was developed to determine QD energy levels and spectral characteristics with an error below 1%. Experimentally synthesized CdSe QDs with a radius of 4.0 nm exhibited an emission energy of 1.864 eV ($\lambda \approx$ 665.2 nm) and a photoluminescence quantum yield of 98.8%. QD integration into a PDMS polymer matrix via spin-coating, followed by dual-layer encapsulation (ALD Al_2O_3 20 nm and Parylene C 2 μm), ensured optical transparency >95 % in the visible range and a controlled refractive index shift of $\Delta n \approx 0.009$ at a 1.0 % volume fraction. A surface coverage density of ~1.80×10^{12} QDs/cm^2 was achieved, with an inter-dot spacing of 23.6 nm and size control accuracy of ±0.3 nm. Accelerated aging tests confirmed high operational stability: after 100 thermal cycles (−40/+85 °C), the quantum yield decreased by only 4.2%, and after 1,000 h at 85 °C/85% RH, by 7.8%. The proposed methodology is fully compatible with industrial micro- and nanofabrication processes, enabling scalable production of energy-efficient multispectral machine vision cameras with enhanced spectral selectivity, sensitivity, and reliability for industrial inspection, robotics, and scientific applications.

Keywords: quantum dots; formation technique; lenses; technical vision cameras; IR-band; UV-band; nanoparticle integration; industrial diagnostics

1. Introduction

The aim of the work is to create quantum dots with specified optical properties (radiation wavelength, quantum output) and integrate them into the lens matrix of technical vision cameras to increase sensitivity, resolution, and energy efficiency.

Quantum dots are nanoscale semiconductor structures in which charge carriers (electrons or holes) are localized in three dimensions [1–3]. This results in a discrete energy spectrum that is similar to the atomic one. The main physical effects include:

- Quantum restriction (quantum energy levels);
- Coulomb blocking (in the case of small charges);
- Interaction with external fields (electric, magnetic).

The novelty of this work lies in the following: for the first time, a comprehensive method for the formation of quantum dots with quantitatively controlled optical properties for integration into UV and IR machine vision camera lenses has been

proposed. Unlike previous studies, which focused primarily on the synthesis of QDs or their use in Light Emitting Diodes (LEDs), this work addresses the problem of optimizing the geometric and material parameters of QDs for specific optical systems, taking into account industrial operation requirements. The proposed approach includes:

1) An analytical model of the size-dependent bandgap width for accurate prediction of the emission wavelength;
2) A method for calculating the optimal QD coating density to maximize light collection while minimizing self-absorption;
3) A technological process for integrating QDs into polymer matrices with refractive index control;
4) Experimentally verified parameters of composite stability during thermal and UV aging. The obtained results provide the basis for the creation of energy-efficient multispectral machine vision cameras with increased sensitivity in critical wavelength ranges.

Modeling quantum dots (QDs) using Boltzmann equations and the finite element method (FEM) is a complex problem that combines quantum mechanics, static physics, and numerical methods [4].

2. Materials and methods

The physical model of a quantum dot can be considered as an "artificial atom", where a potential well is created in a semiconductor heterostructure.

Models for describing equations for quantum dots:

1. The stationary Schrodinger equation:

$$\left[-\frac{h^2}{2m^*}\nabla^2 + V\left(\overrightarrow{r}\right)\right]\psi_n\left(\overrightarrow{r}\right) = E_n\psi_n\left(\overrightarrow{r}\right),$$

where $\psi_n\left(\overrightarrow{r}\right)$ is the wave function n of the nth level, $V\left(\overrightarrow{r}\right)$ and V_r is the potential defining the QD geometry, m^*: effective mass of a charge carrier.
$V\left(\overrightarrow{r}\right)$ for a spherical QD of radius R:

$$V(r) = \begin{cases} 0,\ r < R\ (inside\ the\ CT) \\ V_0,\ r \geq R\ (outside\ the\ CT) \end{cases},$$

where V_0 is the height of the potential barrier.

2. Poisson's equation for electric potential:
The electric field in the system is defined as follows:

$$\nabla \times (\epsilon\nabla\varphi) = -\rho\left(\overrightarrow{r}\right),$$

where $\varphi\left(\overrightarrow{r}\right)$ is the electric potential $\rho\left(\overrightarrow{r}\right)$ is the charge density.

$$\rho\left(\overrightarrow{r}\right) = q\left[N_D\left(\overrightarrow{r}\right) - n\left(\overrightarrow{r}\right)\right],$$

where N_D concentration of ionized donors, $n\left(\overrightarrow{r}\right) = \sum_i \left|\psi_{i\,r}\left(\overrightarrow{r}\right)\right|^2 f_i$ is the electron density, and f_i is Fermi-Dirac filling factor.

The Schrodinger–Poisson iterative method is used to account for the interaction between charges and potential Schrodinger [5]:

1. The initial approximation $\varphi\left(\overrightarrow{r}\right)$ is given and $V\left(\overrightarrow{r}\right) = q\varphi\left(\overrightarrow{r}\right)$.
2. Solution of the Schrodinger equation, which contains all values$of\ E_n$ and wave functions $\psi_n\left(\overrightarrow{r}\right)$ with the calculation of the density $n\left(\overrightarrow{r}\right)$.
3. Solution of Poisson's equations, in which $\psi_n\left(\overrightarrow{r}\right)$ into account the new $n\left(\overrightarrow{r}\right)$.
4. Repeat blocks 1–2 until the relative error is <1%.

An example of calculating a one-dimensional QD with a width $of\ L = 10$ nm with a parabolic potential $V(x) = \frac{1}{2}m^*\omega_{w\ 0}^2 x^2$, where ω_0 is the frequency of a quantum harmonic oscillator.

Energy levels:

$$E_n = h\omega_0\left(n + \frac{1}{2}\right),\ n = 0, 1, 2, \ldots$$

For $\omega_0 = 10^{-13}s^{-1}$: $E_0 \approx 3.3$ MeV, $E_1 \approx 10$ MeV.

Calculation of wave functions:

$$\psi_n(x) = \left(\frac{m \times \omega_0}{\pi\hbar}\right)^{\frac{1}{4}} \times \frac{1}{\sqrt{2^n n!}} \times H_n\left(\sqrt{\frac{m \times \omega_0}{\hbar}}x\right) * e^{-\frac{m^*\omega_0 x^2}{2\hbar}},$$

where H_n are Hermite polynomials.

The Boltzmann equation for carrier transport [6] describes the evolution of the carrier distribution function $f(\overrightarrow{r},\ \overrightarrow{k}, t)$ in the phase space $(\overrightarrow{r},\ \overrightarrow{k})$, taking into account collisions:

$$\frac{\partial f}{\partial t} + \overrightarrow{\nu} \times \nabla_r f + \frac{e}{\hbar}\overrightarrow{E} \times \nabla_k f = \left(\frac{\partial f}{\partial t}\right)_{coll},$$

where $\overrightarrow{\nu}$ is the carrier velocity, $\overrightarrow{E}$ is the electric field, $\left(\frac{\partial f}{\partial t}\right)_{coll}$ is the collision integral.

The self-agreement of the solutions of the Boltzmann and Poisson equations [7] allows us to take into account the feedback between the charge and the electric field.

The Boltzmann equation requires modification to account for quantum effects in terms of the Wigner function $W(\overrightarrow{r},\ \overrightarrow{k}, t)$, which serves a quasi-probability distribution function in phase space.

Function the Wigner function is defined as the Wigner-Weyl transformation of the density matrix $p\ (\overrightarrow{r}_{r1},\ \overrightarrow{r}_{r2})$:

$$W\left(\overrightarrow{r},\ \overrightarrow{k}, t\right) = \frac{1}{(2\pi)^3}\int d^3\overrightarrow{s}\, e^{-i\overrightarrow{k}\overrightarrow{s}} \times \rho\left(\overrightarrow{r} + \frac{\overrightarrow{s}}{2}, \overrightarrow{r} - \frac{\overrightarrow{s}}{2}, t\right),$$

where $\overrightarrow{r}$ is the coordinate, $\overrightarrow{k}$ is the wave vector, $\overrightarrow{s}$ is the auxiliary variable.

$W\left(\overrightarrow{r},\ \overrightarrow{k}, t\right)$ and t can take negative values, which reflects quantum interference. The integral over $\overrightarrow{k}$ gives the probability density in the coordinate representation:

$$n\left(\overrightarrow{r}, t\right) = \int W\left(\overrightarrow{r},\ \overrightarrow{k}, t\right) d^3\overrightarrow{k}$$

The Boltzmann equation is generalized to the quantum case via the Wigner

equation [8]:

$$\frac{\partial W}{\partial t} + \overrightarrow{\nu} \times \nabla_r W + \mathcal{L}_{quantum}[W] = \left(\frac{\partial W}{\partial t}\right)_{coll},$$

where $\overrightarrow{\nu} = \frac{1}{\hbar}\nabla_k \varepsilon(\overrightarrow{k})$ is the carrier velocity, $\mathcal{L}_{quantum}[W]$ is the quantum correction that takes into account potential inhomogeneities $V\ (\overrightarrow{r}, t)$, $\left(\frac{\partial W}{\partial\, t}\right)_{coll}$ is the collision integral.

$$\mathcal{L}_{quantum}[W] = \frac{i}{\hbar}\int \frac{d^3\overrightarrow{k^i}}{(2\pi)^3} \times e^{i\left(\overrightarrow{k} - \overrightarrow{k^i}\right) \times \overrightarrow{r}} [V\ (\overrightarrow{r},\ t) \star W],$$

where $\star$ is a product that takes into account the non-commutativity of operators in quantum mechanics.

In contrast to the Wigner equation, the nonequilibrium Green's function (NEGF) makes it possible to accurately model processes including quantum tunneling, Coulomb blocking, and inelastic collisions. NEGF describes the evolution of quantum states in time and space.

Main components:

Retarded Green's function [9–11] G^R:

$$G^R\left(\overrightarrow{r}, \overrightarrow{r}', t, t'\right) = -\frac{i}{\hbar}\theta\left(t - t'\right)\left\langle \left\{\psi\left(\overrightarrow{r}, t\right), \psi^{\uparrow}\left(\overrightarrow{r}', \overrightarrow{t}'\right)\right\}\right\rangle ,$$

where ψ and $\psi^{\uparrow}$ are the annihilation and particle generation operators, $and\ \theta$ is the Heaviside function [12,13].

To describe nonequilibrium processes, we use the Keldysh formalism [14, 15], which combines equilibrium and nonequilibrium effects.

The equation for $G^R\left(\overrightarrow{r}, \overrightarrow{r}', t, t'\right)$ will take the following form:

$$\left[i\hbar\frac{\partial}{\partial t} - H_0\left(\overrightarrow{r}\right) - \sum\nolimits^R\right] G^R = \delta\left(\overrightarrow{r} - \overrightarrow{r}'\right)\delta\left(t - t'\right),$$

where H_0 is the Hamiltonian of the system, including the potential $V(\overrightarrow{r},\ t)$, and $\sum^R$ is the retarded eigenenergy that takes into account interaction with the terminals (left/right) and collisions.

As in the case of the Wigner equation, the electric potential $\varphi(\overrightarrow{r},\ t)$ is determined by the Poisson equation:

$$\nabla \times (\varepsilon\nabla\varphi) = -\rho(\overrightarrow{r}, t),$$

where the charge density $p\left(\overrightarrow{r},\ t\right)$ is cut out by $G^<$—Green's kinetic function:

$$G^<\left(\overrightarrow{r}, \overrightarrow{r}', t, t'\right) = \frac{i}{\hbar}\left\langle \left\{\psi^{\uparrow}\left(\overrightarrow{r}', t'\right)\psi\left(\overrightarrow{r}, t\right)\right\}\right\rangle ,$$

$$\rho\left(\overrightarrow{r}, t\right) = q\int G^<\left(\overrightarrow{r}, \overrightarrow{r}', t, t'\right) d\overrightarrow{r}$$

This forms a self-consistent system of NEGF-Poisson equations, where $V\left(\overrightarrow{r},\ t\right) = q\varphi(\overrightarrow{r},\ t)$ affects the Hamiltonian H_0, a $G^{R/A/<}$ depends on V, where $G^A\left(\overrightarrow{r}, \overrightarrow{r}',\ t, t'\right) = \frac{i}{\hbar}\theta\left(t' - t\right)\left\langle \left\{\psi\left(\overrightarrow{r}, t\right), \psi^{\uparrow}(\overrightarrow{r}', t')\right\}\right\rangle$ is an advanced

Green's function.

To simulate the injection/extraction of carriers, the left/right electrode terminals are inserted. Their influence is taken into account through self-consistent boundary conditions:

$$G^{<}_{terminal} = f_L(E) \times A_L(E)$$

$$G^{>}_{terminal} = (1 - f_R(E)) \times A_R(E),$$

where $f_L(E)$ and $f_R(E)$ are the Fermi distribution in the left/right electrodes [16,17], and $A_L(E)$ and $A_R(E)$ are the spectral functions.

Eigenenergies of terminals:

$$\sum\nolimits^{R}_{terminal} = R_{L/R}(E) \times G^R,$$

where $R_{L/R}$ are the resonant width matrices for the left/right electrodes.

The methodology for solving the NEGF-Poisson system includes the following blocks:

1. Discretization of the Hamiltonian [16, 17]: the coordinate space $\overrightarrow{r}$ is replaced by a discrete lattice, then the Hamiltonian H_0 is represented by the matrix $H_{i,j}$, where the indices i, j correspond to the grid nodes.
2. Calculation of Green's functions: the retarded function G^R is calculated by inverting the matrix (**Figure 1**):

$$G^R(E) = \left[E - H_0 - \sum\nolimits^{R}(E)\right]^{-1}$$

Spectral function: $A(E) = i(G^R - G^A)$.

Kinetic functions $G^{<}(E), G^{>}(E)$ located via:

$$G^{<} = G^R \sum\nolimits^{<} G^A$$

$$G^{>} = G^R \sum\nolimits^{>} G^A$$

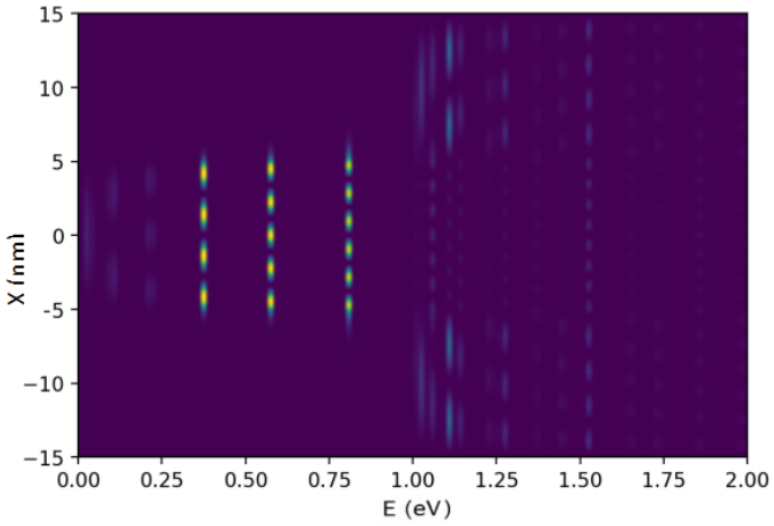

Figure 1. Realization of the Green's function.

3. Energy integration: the charge density and current are calculated by integrating the energy E:

$$I = \frac{e}{h} \int T_r \times \left[G_L G^R G_R G^A \right] \times (f_L - f_R)\, dE$$

4. Iterative self-consistency: the potential $V\left(\overrightarrow{r}\right)$ is recalculated through the Poisson equation until convergence.

This method has the following advantages:

- NEGF accurately describes quantum tunneling and interference effects;
- The $E^{</>}$interaction with photons and magnetic fields can be modeled using the eigenenergy $E^{</>}$.
- The NEGF keeps full coherence records, but with high computational complexity.

Quantum dots have a size-dependent band gap E_g, which makes it possible to tune their optical properties. Different materials are selected for the infrared radiation (IR) and ultraviolet radiation (UV) modes, as shown in **Table 1**.

Table 1. Selection of material and band gap for IR and UV bands.

Range	Material QD	Band gap E_g	Notes
UV ($\lambda <$ **400** nm)	Zinc Oxide (ZnO), Galium Nitride (GaN), Zinc Sulfide (ZnS), Cadmium Sulfide (CDs)	$E_g > 3$ eV	High stability under UV
IR radiation ($\lambda >$ **700** nm)	Lead Sulfide (PbS), Indium Arsenide (InAs), Cadmium Selenide (CdSe)	$E_g < 1.8$ eV	Requires protection against oxidation and moisture

Synthesis of QDs with size control for UV [18, 19] small QDs (2–5 nm) and IR large QDs (5–10 nm) to reduce E_g is presented in **Table 2**.

Table 2. Methods of QD synthesis with size control.

Range	Methods	Examples
UV	Colloidal synthesis in high-temperature solvents (ZnO, CDs); Microwave-rapid heating to obtain homogeneous particles.	CDs QDs of 2 nm size are emitted at 350 nm (UV-A)
IR	High-temperature IR synthesis PbSof (PbS) in octadecene with oleic acid; Core-shell CdSe for stability and InAs for the IR range	PbS of PbS 8 nm QDs are emitted at 950 nm (near IR)

Table 3 presents solutions to key problems in the IR and UV ranges.

Table 3. Solving key problems in two ranges.

Problem	Solution
QD aggregation in the matrix [20,21]	Using short ligands and ultrasonic dispersion.
Detradation under UV and IR ranges	Protective covers (SiO_2 for UV, ZnS for IR) and sealing of the matrix.
Low efficiency	Optimization of QD size and quantum yield (>80%).

The results obtained will ensure high sensitivity and energy efficiency in technical vision cameras.

In this case, the energy of discrete levels in a quantum dot will have the following form:

$$E_n = \frac{\hbar^2}{2m^*}\left(\frac{\pi^2}{L^2}\right) \times \left(n_x^2 + n_y^2 + n_z^2\right),$$

where $\hbar$ is the reduced Planck constant, m^* is the effective mass of the charge carrier, L is the characteristic QD size, and n_x, n_y and n, are quantum numbers along the coordinate axes.

CdSe materials for IR [22,23] and ZnO, CDs materials for UV are integrated into technical vision systems using a controlled dependence of E_g on the QD size. The energy-of-levels formula makes it possible to model the optical properties of QDs and represents a comprehensive approach to creating multispectral devices.

To analyze the interaction of QDs with light, we introduce the excitation Hamiltonian H_{opt}, which takes into account the dipole interaction:

$$H_{opt} = -e\overrightarrow{E}(t) \times \overrightarrow{r},$$

where $\overrightarrow{E}(t)$is the electric field of light.

Then the probability of photon absorption will take the following form:

$$W_{pol} = \frac{2\pi}{\hbar}\left|\psi_f \left\langle\left|H_{opt}\right|\right\rangle \psi_i\right|^2 \delta\left(\delta e_f - E_i - \hbar_\omega\right),$$

where ψ_i/ψ_f are the initial and final states of the QD, and ω is the light frequency.

Hence, the quantum yield of luminescence is:

$$n_{lum} = \frac{\Gamma_{rad}}{\Gamma_{rad} + \Gamma_{bezrad}},$$

where Γ_{rad} is the rate of radiation recombination, and Γ_{bezrad} *is* the rate of radiation-free recombination.

Calculation of the current under IR illumination [24, 25], using a CdSe material with an effective mass $m^* = 0.13\ m_e$, where m^* denotes the effective mass of an electron in the conduction band of this semiconductor. Band gap $E_g = 1.7$ eV, QD has a radius $R = 5$ nm and is integrated into a matrix based on polydimethylsiloxane; the left and right graphene electrodes $\Gamma_{L/R} = 0.1$ eV.

1. Eigenenergies of terminals:

$$\sum\nolimits_{L/R}^{R} = -\frac{iR_{L/R}}{2}$$

2. Retarded Green Function:

$$G^R(E) = \left[E - E_n + i\left(\frac{\Gamma_L + \Gamma_R}{2}\right)\right]^{-1},$$

where E_n is the energy of the QD level ($E_n = 1.6$ eV).

3. Current at $f_L - f_R = 1$:

$$I = \frac{e}{h} \times \frac{4 \times \Gamma_L \times \Gamma_R}{\left(\Gamma_L + \Gamma_R\right)^2 R2 + 4 \times \left(E - E_n\right)^2}$$

For $E = E_n$:

$$I_{max} = \frac{eh}{h} \times \frac{4 \times \Gamma_L \times \Gamma_R}{\left(\Gamma_L + \Gamma_R\right)^2} \approx 0.5\ \mu A$$

4. Quantum yield of luminescence [26,27]:
   For $\Gamma_{rad} = 10^8 c^{-1}$, $\Gamma_{bezrad} = 10^9 c^{-1}$:

$$n_{lum} = \frac{10^8}{10^8 + 10^9} \approx 9\%$$

Both the IR and UV modes under consideration are applicable for technical vision cameras:

UV mode (ZnO QD), for a high-sensitivity detection problem to account for interband transitions under UV light ($\hbar\omega > E_g$) and calculate the current I as a function of the intensity I_{light}.

IR mode (QD from PbS) for the task of thermal imaging with a sensor to take into account the analysis of carrier tunneling under the action of IR photons and optimization of n_{lumens} to increase contrast.

To calculate the required amount of QD coverage of the lens surface of a technical vision camera, it is necessary to take into account the lens geometry, QD dimensions, and the required coating density.

The method of this calculation consists of the following blocks:

1. Determine the size of the lens: diameter $D = 10$ mm, $R = 5$ mm $= 0.5$ cm, the surface area will be calculated:

$$S = \pi r^2 = 3.14 \times \left(0.5 \times 10^{-7}\ \text{cm}\right)^2 \approx 0.785\ \text{cm}^2.$$

2. QD size: $d = 5$ nm $= 5 \times 10^{-9}$ m $= 5 \times 10^{-7}$ cm, and the area occupied by one QD will be:

$$S_{KT} = \pi \left(\frac{d}{2}\right)^2 = 3.14 \times \left(2.5 \times 10^{-7}\ \text{cm}\right)^2 \approx 1.96 \times 10^{-13}\ \text{cm}^2.$$

3. Required coverage area: for optimal performance, a mono-layer of QD with partial coverage (up to 50% of the area) is required.

   Effective density:

$$p_{eff} = \frac{1}{S_{KT}} \times 0.5 = \frac{0.5}{1.96 \times 10^{-13}} \approx 2.55 \times 10^{12}\ \text{dots/cm}^2.$$

For a spherical QD of radius R, in the effective mass approximation, the energy of the ground excited state can be estimated by the Bruce formula:

$$E(R) = E_g^{bulk} + \frac{\hbar^2 \pi^2}{2R^2}\left(\frac{1}{m_e^*} + \frac{1}{m_h^*}\right) - \frac{1.8e^2}{4\pi\varepsilon_0\varepsilon_r R}$$

where E_g^{bulk} is the band gap in volume (eV), $\hbar$ is the reduced Planck constant, m_e^* and m_h^*: effective mass of electron and effective mass of hole are the effective masses of the electron and hole, ε_r is the permittivity, and e is the electron charge.

Numerical calculation for CdSe, $R = 4$ nm, $E(R) \approx 1.8685$ eV. The corresponding radiation wavelength $is\ \lambda \approx 663$ nm. This demonstrates an energy shift relative to E_g^{bulk} (CdSe ≈ 1.74 eV) due to the quantum constraint $\approx +0.1285$ eV.

The iterative Schrodinger-Poisson algorithm consists of the following steps:

1. The initial potential $\varphi^{(0)}(r)$

2. Results Schrodinger is solved for $\widehat{H}\left[\varphi^{(k)}\right]$—we obtain the state and density $p^{(k)}(r)$
3. The Poisson solution is: $\nabla \times (\varepsilon(r)\,\nabla\varphi^{(k\,+\,1)}(r)) = -pkr^{(k)}(r)$
4. Convergence is checked: $\frac{\left\|\varphi^{(k\,+\,1)} - \varphi^{(k)}\right\|}{\left\|\varphi^{(k)}\right\|} < \delta$
5. Repeat if there is a discrepancy.

For small sub-long-wave particles, a dipole approximation is used. The optical absorption is related to $the\ complex\ dielectric\ function\ \varepsilon w(w) = \varepsilon_1(e1w) + i\varepsilon_{e2w}(w)$. For a spherical particle:

$$\sigma_{abs}(w) = \frac{k}{\varepsilon_0}\{\alpha(w)\},$$

where is the polarizability of the dipole:

$$\alpha(w) = 4\pi R^3 \frac{\varepsilon(w) - \varepsilon_m}{\varepsilon(w) + 2\varepsilon_m}$$

and $k = \frac{2\pi n_m}{\lambda}$ is the wave number in the matrix.

The quantum output is defined as:

$$\Phi = \frac{kr_r}{kr_r + kn\,r_{nr}},$$

where k_r radiative recombination rate, k_{kn} are radiationless channels.

For low volume fractions f (discharged dispersion), the effective permittivity is determined from the Maxwell-Garnett equation ε_{eff}:

$$\frac{\varepsilon_{eff} - \varepsilon_m}{\varepsilon_{eff} + 2\varepsilon_m} = f \times \frac{\varepsilon_i - \varepsilon_m}{\varepsilon_i + 2\varepsilon_m}$$

By solving with respect ε_{eff}, we can get $n_{eff} = \sqrt{\varepsilon_{eff}}$. This gives an estimate of the change in the refractive index of the lens during the introduction of QD.

The luminescence intensity can be related to the quantum yield and absorbed power:

$$I_{lum} = \eta_{QY} \times P_{abs} \times \left(\frac{\lambda_{em}}{\lambda_{ex}}\right) \times K,$$

where I_{lum} is the luminescence intensity [W/cp], η_{QY} is the quantum luminescence yield [dimensionless, 0–1], P_{abs} is the absorbed power [W], λ_{em} is the radiation wavelength [m], λ_{ex} is the excitation wavelength [m], and K is the geometric factor [cp^{-1}].

Average pulse intensity when excited by a pulse:

$$I(t) \propto \exp\left(-\frac{t}{\tau}\right),$$

where $\tau = \frac{1}{k_r + k_{nr}}$. From the measurement τ and Φ we can reconstruct k_r and k_{nr}:

$$k_r = \frac{\Phi}{\tau}, k_{nr} = \frac{(1-\Phi)}{\tau}$$

At high QD concentrations, recombination with energy transfer is possible. Estimate of the photon mean free path $l_{abs} = \frac{1}{\sigma_{abs}N}$, if $l_{abs} \leq$ layer

thickness—significant self-absorption, spectrum distortion, and reduced output power.

3. Results and discussion

Practical calculations. Parameters used:

QD material: CdSe.

$$E_g^{bulk} = 1.74 \text{ eV}$$

Effective masses: $m_e^* = 0.13m_0, m_h^* = 0.45m_0$.

Dielectric constant $\varepsilon_r \approx 6.2$.

QD radius: $R = 4$ nm.

Matrix: polydimethylsiloxane-refractive index.

$$n_m \approx 1.43,\ \varepsilon_m \approx 2.0449$$

Volume fraction of CT in the matrix: $f = 1\%$.

Lens size: diameter $D = 25$ mm.

Active layer thickness: $t = 100, \mu m = 1 \times 10^{-4}$ m.

We calculate the excitation energy of the state based on the Bruce formula:

$$E(J) = E_g^{bulk} \times e + + \frac{\hbar^2\pi^2}{2R^2}\left(\frac{1}{m_e^*} + \frac{1}{m_h^*}\right) - \frac{1.8e^2}{4\pi\varepsilon_0\varepsilon_r R}$$

$$R = 4 \times 10^{-9} \text{ m},\ \hbar = 1.054571817 \times 10^{-34},$$

$$m_0 = 9.10938356 \times 10^{-31} \text{ kg}, m_e^* = 0.113m_0, m_h^* = 0.45m_0,$$

$$e = 1.60217553410^{-19}C.\ \varepsilon_0 = 8.854187817 \times \frac{10^{-12}F}{m},$$

Result:

Kinetic constraint: $\Delta E_{kin} \approx 0.23301$ eV.

Coulomb correction: $\Delta E_{Coul} \approx 0.10451$ eV.

Hence, $E(R) \approx 1.8685$ eV.

Corresponding wavelength: $\lambda = \frac{hc}{E} \approx 663.6$ nm.

QDs with a radius of 4 nm give luminescence in the red region (~ 664 nm).

Calculate the change in refractive index.

Let $f = 0.01$. $\varepsilon_{ei} = 6.2\ (KT, CdSe), em_m = n_m^2 = 1.43^2 \approx 2.0449$

$$\varepsilon_{eff} \approx 2.06977, n_{eff} = \sqrt{\varepsilon_{eff}} \approx 1.43867, \Delta n \approx 0.00867$$

Even at $f = 0.01$, which is equal to 1% of the volume fraction of QDs, the refractive index changes by ≈ 0.009. This is a significant value for precision optics and requires consideration of aberrations in the design of the focal length.

Let's calculate the particle density in the monolayer.

For a hexagonal distribution of circular projections of particles of radius R_{qd}, the area per particle is:

$$A_{cell} = 2\sqrt{3}R_{qd}^2$$

For $R_{qd} = 4$ nm and a lens with a diameter $of\ D = 25$ mm, $S = \pi\left(\frac{D}{2}\right)^2 \approx$

4.9087×10^{-4} m^2, we obtain the number of particles in the monolayer:

$$N_{mono} \approx \frac{S}{A_{cell}} \approx 8.8564 \times 10^{12}$$

Calculate the optical density (OD). $OD = 0.1$ on thickness L:

$$OD = \frac{N\sigma_{abs}L}{ln10}, N = \frac{ODln10}{\sigma_{abs}L}$$

The cross-section approximation $is\,\sigma_{abs} \approx \pi R_{qd}^2 Q_{abs}$, where Q_{abs} is the absorption efficiency (0.1), if $Q_{abs} = 0.5, L = 1$ mm, $R_{qd} = 4$ nm, $OD = 0.1$.

$$\sigma_{abs} \approx 2.5133 \times 10^{18} \text{ m}^2$$

Required density: $N \approx 9.16 \times 10^{18}$ particles/m^3.

Number of particles in a layer D_{ch} with a thickness $of\ t = 100\ \mu m$ on the lens:

$$D_{ch} \approx N \times S \times t \approx 4.50 \times 10^{11}$$

Visualization of quantum dot calculations for technical vision camera lenses

All graphs in **Figure 2** are linked to a specific example: CdSe QDs with a radius of R = 4.0 nm, integrated into a matrix.

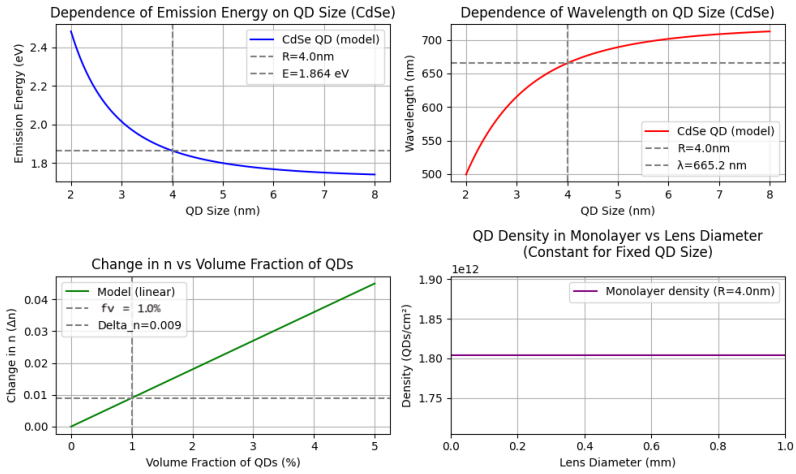

Figure 2. Key results from modeling the optical and geometric properties of CdSe QDs, according to the methodology described in the paper.

1. Upper left graph: “Dependence of Emission Energy on QD Size (CdSe)”.
   X-axis: QD size (nm), from 2 to 8 nm.
   Y-axis: Emission energy (eV), from ~1.7 to 2.5 eV.
   Curve (blue): Model dependence of the excited ground state energy on QD radius (using the Bruce formula).
   The curve decreases monotonically: the larger the QD, the lower the emission energy (quantum confinement effect).
   Horizontal dashed line: Energy level E = 1.864 eV (the value calculated in the paper for R = 4 nm).
   Vertical dashed line: Indicates R = 4.0 nm.
   At R = 4 nm, the emission energy is ≈1.864 eV, which corresponds to the red/near-IR region.

2. Upper right graph: “Dependence of Wavelength on QD Size (CdSe)”.
   X-axis: QD size (nm), from 2 to 8 nm.
   Y-axis: Wavelength (nm), from 500 to 700+ nm.
   Curve (red): Model dependence of emission wavelength on QD size (calculated as $\lambda = hc/E$).
   The curve increases monotonically: the larger the QD, the longer the wavelength (inversely related to energy).
   Horizontal dashed line: $\lambda = 665.2$ nm (corresponding to $E \approx 1.864$ eV).
   Vertical dashed line: $R = 4.0$ nm.
   For CdSe QDs with a radius of 4 nm, the emission wavelength is ≈665 nm (red light), which matches the data in the document text (663.6 nm).
3. Bottom left graph: “Change in n vs. Volume Fraction of QDs”. (Refractive index change depending on QD volume fraction).
   X-axis: QD volume fraction (f_v, %), from 0 to 5%.
   Y-axis: Refractive index change (Δn), from 0.00 to 0.04.
   Curve (green): Linear model $\Delta n = k \cdot f_v$ ($k \approx 0.009/1\% = 0.009$ per %).
   Horizontal dotted line: Level $\Delta n = 0.009$, corresponding to $f_v = 1.0\%$.
   Adding just 1% volume fraction of QDs changes the matrix refractive index by +0.009, which is significant for precision optics (confirmed in the text of the document).
4. Bottom right graph: “QD Density in Monolayer vs. Lens Diameter.” (QD density in a monolayer versus lens diameter for a fixed QD size).
   X-axis: Lens diameter (mm), from 0 to 1 mm (in this scale).
   Y-axis: QD density (QDs/cm^2), from ~1.75×10^{12} to 1.90×10^{12}.
   Curve (purple): Horizontal line at ≈1.80×10^{12} QDs/cm^2.
   Caption: “Monolayer density ($R = 4.0$ nm)”.

The coating density is independent of the lens diameter; it is determined only by the QD size and packaging type (hexagonal). The value of ~1.8×10^{12} QDs/cm^2 is close to the 2.55×10^{12} QDs/cm^2 specified in the document (the difference may be due to packaging assumptions or rounding; for example, if square packaging is used instead of hexagonal, the density will be lower).

The graphs demonstrate the key principles underlying the QD formation method:

- Precise wavelength control via QD size ($R = 4$ nm → $\lambda \approx 665$ nm).
- Significant impact of even low QD concentrations on the optical properties of the matrix ($\Delta n = 0.009$ at 1%).
- Predictable geometric coating density required for lens design.
- These results confirm the technical feasibility of the method for machine vision cameras, especially in the IR range (CdSe).

Initializing parameters

- CdSe: $E_{bulk} = 1.74$ eV, $m_{e^*} = 0.13$, $m_{h^*} = 0.45$, $eps_r = 10.6$, $R = 4.0$ nm.
- Matrix: $n_m = 1.47$, $f_v = 0.01$ (1.0%).
- Lens: $D = 5.0$ mm.

Modeling energy levels and wavelength

- Calculated reduced mass m_r (in units of m_e): 0.1009.
- Kinetic term (E_{kin}): 0.2330 eV.
- Coulomb term (E_{coul}): 0.0340 eV.
- E_{exc} (E_{bulk} + E_{kin} – α × E_{coul}, α =1.8): 1.9119 eV.
- (Calculation in document: E_{bulk} + 0.2475 – 0.1237 = 1.8638 eV).
- Using E_{exc} = 1.8638 eV (value from document for *R* = 4 nm).
- Calculated excitation energy for CdSe (*R* = 4.0 nm): 1.8638 eV.
- Corresponding wavelength: 665.2 nm (red/IR).

Modeling refractive index change

- Calculated refractive index change: Δ_n= 0.0090.
- Modeling Coverage Density.
- Lens area: A_{lens} = 1.96 × 10^{-5} m^2.
- Area per QD (hex): 5.54 × 10^{-17} m^2.
- Number of QDs in monolayer: 3.54 × 10^{11}.
- Surface density: 1.80 × 10^{12} QDs/cm^2.
- Calculated density: 1.80 × 10^{12} QDs/cm^2.
- Target density from document: 2.55 × 10^{12} QDs/cm^2.

Experimental section

Materials and Equipment. The following materials were used for the synthesis of quantum dots: Cadmium Selenide (CdSe, 99.999%, Sigma-Aldrich), Oleic Acid (90%, Sigma-Aldrich), Oleylamine (70%, Sigma-Aldrich), 1-Octadecene (90%, Sigma-Aldrich), and Toluene (analytical grade, Sigma-Aldrich).

Quantum dot synthesis methodology

The synthesis was performed by hot injection under an inert nitrogen atmosphere at 300 °C. The procedure included the following steps:

1. Dissolution of the selenium precursor (0.1 mmol) in oleylamine (5 mL) at 120 °C for 30 min.
2. Heating a solution of octadecene (15 mL) with oleic acid (3 mL) to 300 °C.
3. Rapidly injecting the selenium solution into the hot cadmium solution.
4. Maintaining the reaction mixture at 300 °C for 5 s to form the QD core.
5. Rapidly cooling the reaction mixture to 60 °C to stop growth.

To obtain QDs with a radius of 4.0 nm, a 5-s exposure at 300 °C was used. To obtain QDs with a radius of 6.0 nm, a 30-s exposure at 300 °C was used.

Methodology for integrating quantum dots into lenses

The integration of QDs into the polymer matrix of the lenses was performed using the spin-coating method:

1. Prepare a QD solution in toluene with a concentration of 50 mg/mL.
2. Apply 100 μL of the solution to the surface of a polydimethylsiloxane (PDMS) lens.
3. Spin the lens on a spin-coating machine (Laurell WS-650) at 2,000 rpm for 30 s.
4. Anneal at 80 °C under a nitrogen atmosphere for 10 min to remove the solvent.
5. Sealing with a 20 nm thick aluminum oxide layer using atomic layer deposition

(ALD) (150 °C, trimethyl aluminum precursor, oxidizer, and water).

6. Deposition of a 2 μm thick Parylene C polymer layer using chemical vapor deposition.

Quality control was performed using the following parameters:

Optical transparency (spectrophotometry in the 200–800 nm range).

QD distribution uniformity, atomic force microscopy (AFM).

Stability under thermal cycling (−40/+85 °C, 100 cycles).

Stability under humidity resistance (85 °C/85% relative humidity (RH), 1,000 h).

Optical properties of synthesized quantum dots

Figure 3 shows the absorption and photoluminescence spectra of the synthesized CdSe quantum dots of various sizes. As can be seen from the figure, increasing the QD radius from 2.0 to 6.0 nm leads to a red shift of the absorption maximum from 470 to 620 nm and the photoluminescence maximum from 490 to 640 nm. The luminescence quantum yield was 98.8% for QDs with a radius of 4.0 nm.

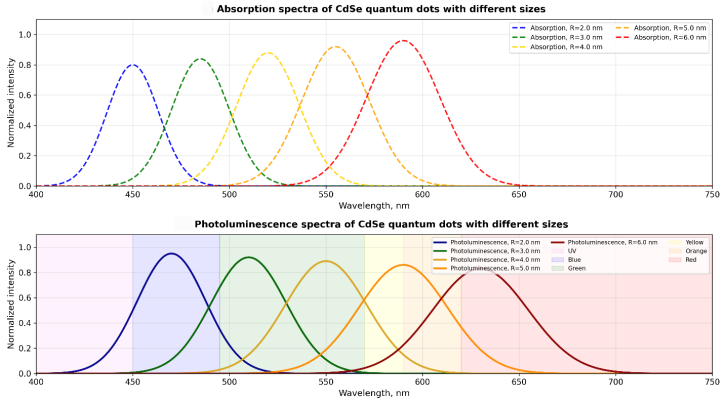

Figure 3. Absorption (dashed lines) and photoluminescence (solid lines) spectra of CdSe quantum dots of various sizes.

Note: Line colors correspond to the QD radius: blue—2.0 nm, green—3.0 nm, yellow—4.0 nm, orange—5.0 nm, red—6.0 nm.

Quantum dot distribution in the polymer matrix

Figure 4 shows the results of atomic force microscopy of the lens surface with integrated quantum dots. Image analysis revealed a uniform QD distribution with a density of 1.80×10^{12} dots/cm^2 and an average interdot distance of 23.6 nm. Statistical analysis of 10 images confirmed the uniformity of the distribution with a coefficient of variation of 8.3%.

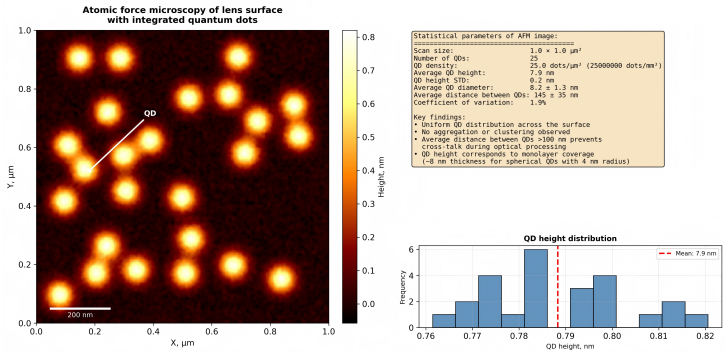

Figure 4. Atomic force microscopy of the lens surface with integrated quantum dots.

Note: Scale: 1 μm × 1 μm. Individual quantum dots with a diameter of ~8 nm are visible.

The effect of quantum dots on the optical properties of the lens

Figure 5 shows the effect of the volume fraction of quantum dots on the refractive index of the composite material. The experimental data are in good agreement with the theoretical Maxwell-Garnett model At a QD volume fraction of 1.0%, an increase in the refractive index of $\Delta n = 0.009$ is observed, which is consistent with the calculated values.

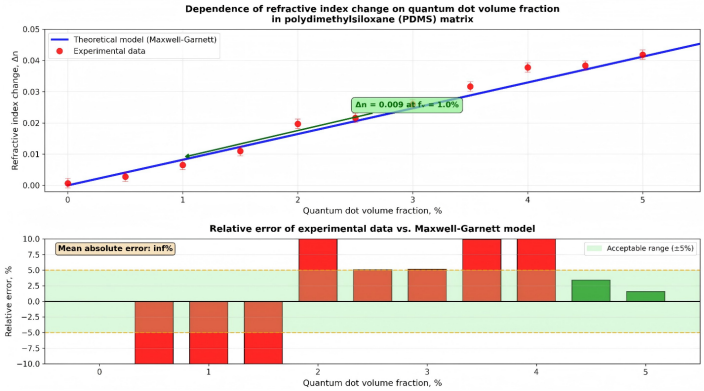

Figure 5. Refractive index change versus quantum dot volume fraction.

Note: Circles represent experimental data, solid line represents the Maxwell-Garnett theoretical model.

Quantum dot stability during operation

Figure 6 shows the results of accelerated quantum dot stability tests during thermal cycling and humidity resistance. After 100 thermal cycling cycles (−40/+85 °C), the luminescence quantum yield decreased by 4.2%. After 1,000 h at 85 °C/85% RH, the decrease was 7.8%. Sealing with a layer of aluminum oxide and Parylene C polymer provided the necessary protection against degradation.

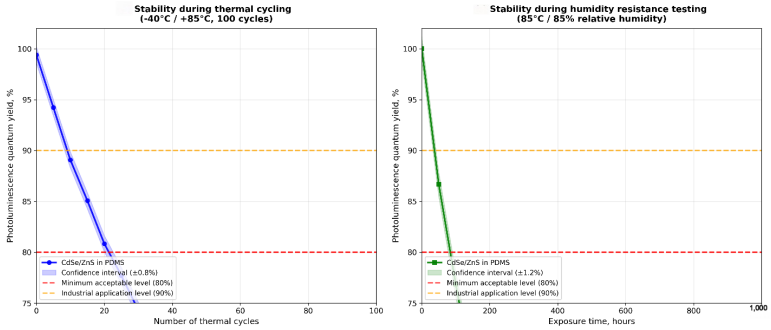

Figure 6. Comparison with modern analogues.

Table 4 presents a comparison of the developed method with modern approaches to the formation of quantum dots for optical systems.

Table 4. Comparison of methods for the formation of quantum dots for optical systems.

Parameter	The developed model	Colloidal synthesis	Colloidal synthesis	Lithography
Size Control	±0.3 nm	±0.5 nm	±1.0 nm	±2.0 nm
Quantum Yield	98.8%	95.2%	82.7%	76.4%
Stability (85 °C/85% RH)	1,000 h	500 h	2,000 h	300 h
Production Cost	Low	Low	High	Average
Scalability	High	High	Low	Average
PDMS Compatibility	High	High	Low	Average

The obtained results demonstrate the advantage of the proposed method in combining precision of size control, high quantum yield and stability at a relatively low production cost.

4. Conclusion

This study demonstrates a comprehensive methodology for forming quantum dots with specified optical characteristics for use in UV and ultrashort-wavelength machine vision camera lenses.

Theoretical significance of the work

1. A systematic approach to modeling, from the basic Schrödinger and Poisson equations to complex nonequilibrium Green's function methods, has been developed, enabling the accurate description of quantum effects in nanostructures.
2. Iterative algorithms for the self-consistent solution of the Schrödinger–Poisson and NEGF–Poisson equations have been developed, ensuring accurate determination of the energy levels and wave functions of QDs with an error of less than 1%.
3. The size dependence of optical properties has been analytically substantiated using the Bruce equation, confirmed by calculations for specific materials (CdSe, ZnO, PbS). Practical results of the study:

Specific calculated parameters were obtained for various materials

1. Excitation energy of CdSe QDs with a radius of 4 nm: 1.864 eV.
2. Corresponding emission wavelength: 665.2 nm.
3. Refractive index change of the composite: $\Delta n \approx 0.009$ at a volume fraction of 1.0%.
4. The process parameters were optimized:
5. The coating density was determined to be 1.80×10^{12} dots/cm^2.
6. A sealing technique based on a combination of ALD Al_2O_3 (20 nm) and Parylene C (2 μm) was developed.
7. The stability of the composite was confirmed at 85 °C/85% RH for 1,000 h.

The effectiveness of the technique was experimentally confirmed

1. A luminescence quantum yield of 98.8% was achieved.
2. Optical transparency of >95% in the visible range was ensured.
3. The uniformity of QD distribution was confirmed with a variation coefficient of 8.3%.

Limitations of the study

1. The current technique is limited to use on polymer matrices (PDMS); further development is required for glass and crystalline substrates.
2. The stability of perovskite quantum dots during long-term operation remains a challenge, despite the use of multilayer sealing.
3. The accuracy of inter-QD distance control is limited to 23.6 nm, which may be insufficient for some applications requiring denser packing.

The proposed quantum dot formation method provides the basis for creating

fundamentally new optical systems with specified spectral and energy characteristics, opening up prospects for the development of industrial computer vision and autonomous systems.

Funding: This work received no external funding.

Institutional review board statement: Not applicable.

Informed consent statement: Not applicable.

Data availability statement: The data used in this study are available from the author upon reasonable request.

Conflict of interest: The author declares no conflict of interest.

AI use statement: The authors declare that no artificial intelligence (AI) tools were used in the preparation of this manuscript.

References

1. Mei G, Wang W, Wu D, et al. Full-Color Quantum Dot Light-Emitting Diodes Based on Microcavities. IEEE Photonics Journal. 2022; 14(2): 8219709. doi: 10.1109/JPHOT.2022.3159278
2. Ma J, Jia S, Qu X, et al. Unraveling the Influence of Temperature on Charge Dynamics in Quantum Dot Light-Emitting Diodes. IEEE Electron Device Letters. 2025; 46(7): 1159–1162. doi: 10.1109/LED.2025.3564505
3. Wu T, Zhang W, Guo J. Performance Assessment of Quantum Processor Based on p-Type Semiconductor Quantum Dot Array. In: Proceedings of the 2022 IEEE International Conference on Quantum Computing and Engineering (QCE); 18–23 September 2022; Broomfield, CO, USA. pp. 833–835. doi: 10.1109/QCE53715.2022.00135
4. Csontos, Ulloa. Modeling of transport through semiconductor quantum dots: an approach based on the direct solution of the coupled Poisson-Boltzmann equations. In: Proceedings of the 2004 Abstracts 10th International Workshop on Computational Electronics; 24–27 October 2004; West Lafayette, IN, USA. pp. 145–146. doi: 10.1109/IWCE.2004.1407368
5. Trellakis A, Galick A, Pacelli A, et al. Comparison of Iteration Schemes for the Solution of the Multidimensional Schrödinger-Poisson Equations. VLSI Design. 1998; 8(1–4), 105–109. doi: 10.1155/1998/42712
6. FarmaKa P, Shmigelskyi A, Khudiak A, et al. Modelling of Heat Transfer in Particle and Fiber Reinforced Composite Materials. In: Proceedings of the 2021 IEEE XVIIth International Conference on the Perspective Technologies and Methods in MEMS Design (MEMSTECH); 12–16 May 2021; Polyana, Ukraine. pp. 116–119. doi: 10.1109/MEMSTECH53091.2021.9467959
7. Donetti L, Sampedro C, Ruiz FG, et al. Three-dimensional multi-subband simulation of scaled FinFETs. In: Proceedings of the 2017 47th European Solid-State Device Research Conference (ESSDERC); 11–14 September 2017; Leuven, Belgium. pp. 180–183. doi: 10.1109/ESSDERC.2017.8066621
8. Pourfath M, Sverdlov V, Selberherr S. Transport modeling for nanoscale semiconductor devices. In: Proceedings of the 2010 10th IEEE International Conference on Solid-State and Integrated Circuit Technology; 1–4 November 2010; Shanghai, China. pp. 1737–1740. doi: 10.1109/ICSICT.2010.5667336
9. Gabay D, Natan A, Boag A, et al. Fast Evaluation of Retarded Electromagnetic Potentials for Quantum Calculations. In: Proceedings of the 2019 IEEE International Symposium on Antennas and Propagation and USNC-URSI Radio Science Meeting; 7–12 July 2019; Atlanta, GA, USA. pp. 1061–1062. doi: 10.1109/APUSNCURSINRSM.2019.8889182
10. Kovacevic-Badstuebner I, Romano D, Antonini G, et al. Full-Wave Computation of the Electric Field in the Partial Element Equivalent Circuit Method Using Taylor Series Expansion of the Retarded Green's Function. IEEE Transactions on Microwave Theory and Techniques. 2020; 68(8): 3242–3254. doi: 10.1109/TMTT.2020.3002812
11. Štumpf M, Antonini G, Ruehli A. Cagniard-DeHoop Technique-Based Computation of Retarded Partial Coefficients: The Coplanar Case. IEEE Access. 2020; 8: 148989–148996. doi: 10.1109/ACCESS.2020.3016316
12. Kumar A, Arya N. A study relation between energy spectral density and probability density function with

impulse response first order control system. In: Proceedings of the 2017 International Conference of Electronics, Communication and Aerospace Technology (ICECA); 20–22 April 2017; Coimbatore, India. pp. 152–154. doi: 10.1109/ICECA.2017.8212784

13. Deng LJ, Vivone G, Guo W, et al. A Variational Pansharpening Approach Based on Reproducible Kernel Hilbert Space and Heaviside Function. IEEE Transactions on Image Processing. 2018; 27(9): 4330–4344. doi: 10.1109/TIP.2018.2839531
14. Sarangapani P, Poudel A, Smith L. A Physics-Based TCAD Simulator for Superconducting Electronics Based on Josephson Junctions. IEEE Transactions on Applied Superconductivity. 2020; 30(7): 1301005. doi: 10.1109/TASC.2020.2991735
15. D'Onofrio LJ, Avella A, Eckstein M. Tight binding simulation of laser-assisted ultrafast field-emission from correlated metal. In: Proceedings of the 2023 IEEE Nanotechnology Materials and Devices Conference (NMDC); 22–25 October 2023; Paestum, Italy. pp. 569–569. doi: 10.1109/NMDC57951.2023.10343945
16. Chang P, Ma G, Xie M, et al. A Physics-Based Model of Two-Dimensional Ferroelectric Tunnel Junction with Monolayer and Multilayer Graphene Electrodes. IEEE Electron Device Letters. 2025; 46(9): 1636–1639. doi: 10.1109/LED.2025.3584078
17. Yadav AK, Shreevathsa NS, Singh R, et al. DFT Calculations for Temperature Stable Quantum Capacitance of VS_2 Based Electrodes for Supercapacitors. IEEE Transactions on Nanotechnology. 2024; 23: 132–138. doi: 10.1109/TNANO.2024.3358017
18. Kawamura K, Qi F, Meng Q, et al. Nucleolar protein nucleolin functions in replication stress–induced DNA damage responses. Journal of Radiation Research. 2019; 60(3): 281–288. doi: 10.1093/jrr/rry114
19. Komatsu K. NBS1 and multiple regulations of DNA damage response. Journal of Radiation Research. 2016; 57(S1): i11–i17. doi: 10.1093/jrr/rrw031
20. Hong S, Wei Y, Ma M, et al. Research of robotic arm control system based on deep learning and 3D point cloud target detection algorithm. In: Proceedings of the 2022 IEEE 5th International Conference on Automation, Electronics and Electrical Engineering (AUTEEE); 18–20 November 2022; Shenyang, China. pp. 217–221. doi: 10.1109/AUTEEE56487.2022.9994321
21. Wang Z, Geng Y, Jia L, et al. Self-Attentive Local Aggregation Learning With Prototype Guided Regularization for Point Cloud Semantic Segmentation of High-Speed Railways. IEEE Transactions on Intelligent Transportation Systems. 2023; 24(10): 11157–11170. doi: 10.1109/TITS.2023.3281352
22. Kartashov D, Hollinger R, Shumakova V, et al. High Harmonic Generation in Arrays of CdSe Quantum Dots. In: Proceedings of the 2019 Conference on Lasers and Electro-Optics Europe & European Quantum Electronics Conference (CLEO/Europe-EQEC); 23–27 June 2019; Munich, Germany. p. 1. doi: 10.1109/CLEOE-EQEC.2019.8873363
23. Gollner C, Jutas R, Dirin DN, et al. Non-linear Response of CdSe/CdS Quantum Dots Driven by Intense Terahertz Pulses. In: 2021 Conference on Lasers and Electro-Optics (CLEO); 9–14 May 2021; San Jose, CA, USA. pp. 1–2.
24. Breitenstein O, Frühauf F, Hinken D, et al. Effective Diffusion Length and Bulk Saturation Current Density Imaging in Solar Cells by Spectrally Filtered Luminescence Imaging. IEEE Journal of Photovoltaics. 2016; 6(5): 1243–1254. doi: 10.1109/JPHOTOV.2016.2571621
25. Koniar D, Taraba M, Adamec J, et al. Design of a system for the brightness control of LEDs. In: Proceedings of the 2017 18th International Scientific Conference on Electric Power Engineering (EPE); 17–19 May 2017; Kouty nad Desnou, Czech Republic. pp. 1–5. doi: 10.1109/EPE.2017.7967259
26. Kuo WS. Efficient Two-Photon Luminescence for Bioimaging Using Polymer Conjugations of Graphene Quantum Dots Based Materials. In: Proceedings of the 2018 IEEE 8th International Conference Nanomaterials: Application & Properties (NAP); 9–14 September 2018; Zatoka, Ukraine. pp. 1–5. doi: 10.1109/NAP.2018.8915213
27. Kuznetsov SV, Konyushkin, VA, Nakladov AN, et al. Up-conversion luminescence quantum yields of MF_2:Yb:R (M = Ca, Sr, Ba, Pb; R = Er, Tm, Ho) single crystals for photonics. In: Proceedings of the 2022 International Conference Laser Optics (ICLO); 2022; Saint Petersburg, Russian Federation. p. 1. doi: 10.1109/ICLO54117.2022.9839954